

Plume-Induced Flow Separation over a Cone-Cylinder Flare Body

James E. Kless* and Goetz H. Klopfer†

NASA Ames Research Center, MS 258-2, Moffett Field, CA 94035

The extent of boundary-layer separation due to the presence of a jet plume was studied for a cone-cylinder-flare configuration using the Overset Navier-Stokes CFD code, OVERFLOW. Simulations were made at a free-stream Mach number of 4.65 for nozzle exit pressure to free-stream pressure ratios ranging from jet off to 168. CFD results were obtained assuming a fully laminar boundary layer, fully turbulent boundary layer, and a laminar-turbulent transitional boundary layer. The one-equation Spalart-Allmaras (SA) and the two-equation SST model were compared for the turbulent cases. The effect of wall boundary conditions was studied by comparing the isothermal wall to the adiabatic wall conditions. CFD results were compared to existing experimental data obtained from the Langley Unitary Plan wind tunnel. The results indicate strong plume-induced flow separation when modeled as fully laminar and weak separation, if at all, when modeled as fully turbulent. The best agreement with experimental results was achieved when the trip location was placed near the end of the flare. The adiabatic wall boundary condition best suited the wind tunnel experiment. However predicting the extent of the plume induced flow separation with numerical simulations is still unreliable due to the extreme sensitivity of the flow field to turbulence models, boundary conditions, and nozzle pressure ratios.

*Aerospace Engineer, STC Corporation, Hampton, VA, and AIAA Member.

†Research Scientist, NASA Ames Research Center, Moffett Field, CA.

Nomenclature

| | |
|-----------------|---|
| A_e | nozzle exit area, sq in. |
| A_t | nozzle throat area, sq in. |
| d | diameter of model forebody, in. |
| l | length of model, in. |
| M_j | exit Mach number of the jet |
| M_∞ | free-stream Mach number |
| P_j | jet exit static pressure, lbf/sq in. |
| P_∞ | free-stream static pressure, lbf/sq in. |
| $PIFS$ | plume induced flow separation |
| R | radius of cylinder, in. |
| $Re_{l,\infty}$ | free-stream Reynolds number based on model length |
| X_s | start of boundary-layer separation, measured from configuration nose in axial direction, in. |
| α | angle of attack, deg |
| γ_j | jet specific heat ratio |
| γ_∞ | free-stream specific heat ratio |
| T_∞ | free-stream temperature, Rankine |
| δ_j | initial inclination of jet boundary at nozzle lip, measured with respect to nozzle center line, deg |
| θ_s | angle measured between separated boundary layer and model surface, deg |

I. Introduction

DURING the ascent phase, rockets traveling at supersonic speeds at high altitudes produce large underexpanded plumes which, under the right conditions, can detach the boundary layer well upstream of the plume. Physically, this is caused by the oblique shock formed by the exhaust plume expansion. The adverse pressure gradient interaction with the boundary layer causes the flow to separate upstream of the nozzle exit plane. The extent of this separation can be important since the separated flow interferes with aerodynamic stabilizing surfaces such as flares and fins typically located in the separated region. In addition, hot plume gases can become entrained in the separation region causing potential structural damage and interfere with communication devices located in these regions. Evidence of this process has been seen on the Saturn V rocket and on the Space Shuttle Solid Rocket Boosters.^{1–5} The goal of the present study was to investigate the capability of the Navier-Stokes flow solver, OVERFLOW⁶ of accurately predicting the phenomenon of boundary layer plume-induced flow separation (PIFS) over rocket geometries. In particular, we validate OVERFLOW against a simple geometric rocket test vehicle for which extensive wind tunnel data are available. Test data for axisymmetric cone-cylinder-flare geometries was generated during the Apollo program. Some of these tests were run at zero pitch and yaw and the flow is essentially axisymmetric. The assumption of axisymmetric flow lessens the need for extensive computational resources for the validation process.

In the following sections we describe the details of the PIFS flow field, the experimental data, the parameters quantifying the flow field, the geometry, the grid generation process and the flow solver. Results are presented and finally, summary remarks are made.

II. Description of the ‘Plume-Induced Separated Flow Field’

During the ascent phase of the Ares 1 launch vehicle,⁷ the exhaust plume of the solid rocket booster or, after stage separation, the J2-X motor of the upper stage is underexpanded and will respond to the low atmospheric pressure to form a large expanded plume. This exhaust plume expands through a Prandtl-Meyer (P-M) expansion. Due to this expansion the free stream flow is deflected by a conical flow compression. The balance between the pressures after the P-M expansion and the conical flow compression of the free stream determines the plume expansion and free stream deflection angle. The P-M expansion depends on the ratio of the nozzle exit pressure to free stream pressure as well as the gas properties of the plume and free stream flows. Assuming multi-species perfect gas flow, the pressure and the expansion after the P-M expansion will increase with increasing ratios of free stream to plume specific heat (γ) ratios. Assuming inviscid flow for the moment, the supersonic free stream is deflected either through an attached oblique shock or a detached bow shock depending on the plume expansion angle. In both cases the aft portion of the shock wave intersects the plume shear layer causing another complicated flow feature downstream of the nozzle exit plane. For viscous flow and both types of shocks the upstream portion of the shocks interact with the free stream boundary layer. Depending on the strength of the adverse pressure gradient produced by the shocks, the on-coming upstream flow can separate. A new oblique shock wave forms due to boundary layer separation and a separated flow region forms upstream of the nozzle exit plane. The extent of the separated flow region depends on the Reynolds number of the flow field. As shown in Fig. 1 the separated flow region is bounded by the solid surface downstream of the separation point, the shear layer also emanating from the separation point, and the expanded plume shear layer. This plume shear layer will entrain fluid from the separated flow region as well as inject plume flow into the separation zone if the flow is turbulent. Large amounts of entrainment will reduce the pressure in the separated flow region and reduce its extent.

The PIFS flow field is complicated and computationally challenging. The plume expansion angle and pressure, the shock boundary layer interaction, and the entrainment of the separated region flow by the plume shear layer are all critical for accurate prediction of the PIFS phenomena. Shear layers are difficult to simulate numerically and require adequate grid resolution and appropriate turbulence models. A turbulent model that does well for both shock boundary layer interaction and entrainment by high energy shear layers of the expanded plume is problematic. In addition it is not clear how the intersection of the separated boundary layer shock and the plume shear layer affects the entrainment of the separated flow, if at all.

The separation location is sensitive to several parameters, including the plume pressure ratios, the gas properties of the two flow streams, turbulence levels and models, transition location, boundary conditions, and configurational geometry. To make the problem tractable we choose laminar flow experimental data for validating the CFD results. However as will be shown later the plume flow cannot be laminar and turbulent models with several corrections will be investigated. In addition, several types of wall boundary conditions will also be studied to assess the sensitivity of these boundary conditions to the extent of the PIFS region.

III. Experimental Data

During the Apollo program extensive wind tunnel testing was done to obtain the aerodynamic data needed. Included in the program were wind tunnel tests conducted at NASA Langley to study the effects of plume induced flow separation on the aerodynamic performance of the Saturn V launch vehicles. The data from these tests are widely available in the open literature.

III.A. The Experiment and Assumptions

A series of cone-cylinder-flare geometries were tested in the Langley 11-inch hypersonic tunnel at Mach 9.65 and in the Langley Unitary Plan wind tunnel at Mach 4.65.¹ The Reynolds numbers based on model length varied from 317,000 to 582,000. The tests were to determine the influence of free stream Mach number, nozzle and flare geometry, angle of attack, nozzle pressure ratios, and nozzle exit Mach numbers on the extent of the separated flow region. The test nozzles were powered with compressed air and were designed to simulate the jet exhaust of a solid-propellant rocket motor operating at altitudes between 165,000 and 215,000 feet.

The test article is shown in Fig. 2. The test report covers a wide range of different model geometries. Included are a range of cone half-angles of different flare (aft skirt) and nozzle geometries. We chose the configuration which has the closest approximation to the Ares 1 launch vehicle for our validation study. It consists of a nine degree half-angle nose cone, a straight cylindrical midsection, and an aft skirt with a flare

half-angle of 13 degrees. The nozzle aft of the flare has a semi-divergence angle of 26 degrees to simulate the initial plume expansion angle of a solid rocket motor. The flare half-angle of the outer nozzle wall is 15 degrees. The model length is 5.82 inches. The entire model is mounted on a strut and sting through which pressurized air is supplied to the nozzle plenum chamber. The test model is polished and the Reynolds numbers are low enough so that the flow over most of the model can be assumed to be laminar. The effect of the boundary layer separation point on the model with Reynolds numbers followed the known trends of boundary layer separation for laminar flat plates and thus verifies that the flow was indeed laminar. The report does state that the plume flow was probably transitional but no data were presented to verify that claim. The stated accuracies of the measured experimental data are as follows: $M_\infty = \pm 0.02$, $X_s = \pm 0.05$ inches, $\delta_j = \pm 5^\circ$, $\theta_s = \pm 0.25^\circ$, and $p_j/p_\infty = \pm 3\%$.

For validating the Overflow code we chose this experimental data since the plumes simulated in this test had pressure ratios similar to the plume expansion ratios for the Ares 1 at the stage separation altitude. In addition the laminar flow condition greatly simplifies the issue of turbulence modelling. The use of compressed air for the plume flow eliminates the need of simulating multi-species plume/free stream flows. The free stream Mach number in the NASA Langley Unitary Plan Wind Tunnel¹ best matched the Mach numbers of the Ares 1 stage separation, so this is the only data that will be used for the code validation.

The data obtained in the test were in the form of Schlieren photographs from which separation location, plume expansion angles, boundary layer separation angles, and separation shock angles were recorded. With these photographs the separation location could not be measured directly. They were inferred by extrapolating the shock separation angle to the surface of the model. The assumption is that the extrapolation gives the correct location of the separation point. The numerical simulations presented in this paper will determine the validity of this assumption. The nozzle pressure ratios and Mach numbers were measured, but neither skin friction nor surface pressure measurements were reported.

III.B. Matching Experimental Flow Conditions

The free-stream pressure and temperature were computed from the Langley Unitary Plan wind tunnel standard operating stagnation pressure and stagnation temperature of $P_o = 16.04$ psi and $T_o = 150^\circ F$ using isentropic, perfect gas assumptions.¹⁰ The freestream Reynolds numbers based on the model length were matched exactly. All free-stream conditions that were used in the simulation are shown in Table 1. The following nominal exit pressure ratios were simulated: $\frac{P_j}{P_\infty} = \text{jet off}, 5, 13, 25, 36, 50, 73, 127, 168$.

The nozzle exhaust exit pressure to free stream pressure ratios (i.e. $\frac{P_j}{P_\infty}$) were matched to the experimental values as follows. With the correct nozzle geometry and free-stream conditions, the nozzle chamber conditions were computed by using 1-D isentropic gas flow theory through a converging-diverging nozzle. These computed chamber conditions were then prescribed at the nozzle plenum chamber inlet and the nozzle flow is simulated with the flow solver. The area-weighted averaged exit pressures are compared to the nominal values and the chamber pressures are adjusted accordingly. This process was iteratively continued until the exit conditions matched the nominal pressures as closely as possible. The final calculated chamber conditions were then used as the inlet boundary condition at the nozzle chamber inlet for the global flow field simulation. The gas in the nozzle was modeled as cold air ($\gamma = 1.4$).

III.C. Flow Separation Parameters

The parameters which represent the extent of flow separation can be found in Fig. 1. X_s was measured using two different methods. In the first method, the flow separation shock wave was extrapolated to the surface of the forebody and the intersection of the extrapolation line and the surface was deemed to be the separation point. In the second, skin friction patterns in the vicinity of the separation were examined to identify the point where the flow detaches from the body effectively locating the separation point on the body. The initial angle of inclination of the nozzle flow, δ_j , was measured by the angle between the tangent line to the initial part of the jet (estimated using both streamline patterns and density gradient magnitude contours) and the center-line.

IV. CFD Procedure

IV.A. Grid Generation

The Overset Grid System used for this simulation was generated using the Chimera Grid Tools Script Library version 2.0b.⁸ A schematic of the cone-cylinder-flare body can be found in Fig. 2. The mesh is axisymmetric with a $\pm 1^\circ$ rotation about the center-plane. The complete mesh consists of a near body grid which spans the entire length of the model, a collar grid to resolve the nozzle/skirt junction, a nozzle grid, a plume grid, and an off-body outer box grid. The maximum stream-wise spacing along the body was 0.08 percent of the total length of the model. Large streamwise refinement was necessary in accurately predicting the separation location. The initial wall normal spacing for the near body grids was based on a $y^+ \approx 1$. The mesh consists of 5 zones with a total of 2.9 million grid points. Details of the dimensions for each of the zones can be found in Table 2. Fig. 3 shows the mesh used in the simulation. The grid system spacings and methodology was based on the Overset best practices established by Chan, et al.⁹

IV.B. Flow Solver

The flow solver that was used for this simulation was the structured grid Overset Navier-Stokes code OVERFLOW version 2.1v.⁶ All simulations were run in steady state mode at a zero angle of attack. A three factor alternating direction implicit (ADI) block tridiagonal scheme (developed by Beam and Warming) along with central differencing for the Euler terms was used for all cases. The TLNS3D dissipation scheme was used to increase convergence rates. Viscous wall (no slip) boundary conditions were applied to all solid surfaces. The uniform flow was prescribed at the nozzle chamber inlet face with the pressure prescribed as detailed in the previous section. The symmetry axis was modeled as an inviscid wall (slip) condition. Free-stream conditions were imposed at the upstream and far field boundary while a zeroth-order extrapolation outflow condition was imposed on the downstream far field boundary. The simulations were run for 38,000 time steps in steady-state mode to achieve a 3-4 order of magnitude drop in the residuals. The maximum CFL number was ramped up from 1 to 5 over 25,000 time steps. Log plots of the L2-norm of the residuals can be found in Fig. 4 for the six pressure ratios and laminar flow conditions.

Separate computations were made assuming a fully laminar flowfield to match the stated experimental flow conditions, a fully turbulent flowfield to investigate the effects of turbulence, and a transitional flowfield to attempt to match the experimental data more accurately. Since OVERFLOW does not have a transitional model, the transitional flowfield analysis was done by separately placing 4 different trip locations on the rocket surface. The "trip" locations determine the transition from laminar to fully turbulent flow. The first trip location was placed at the midpoint of the flare, the second was placed at the end of the flare, the third at the midpoint of the nozzle, and the fourth was placed at the exit of the nozzle. The turbulence models used for these and the fully turbulent computations are discussed in the following section.

IV.C. Turbulence Models

The two turbulence models used in the simulation were the one-equation Spalart-Allmaras (SA) and the two-equation Shear Stress Transport (SST) [Mentor, 1993] models. The flow solver OVERFLOW⁶ includes options for including the following correction terms for the SST model: (1) SARC form of rotational/curvature correction (2) Sarkar Compressibility Correction and (3) Abdol-Hamid Temperature Correction.

IV.D. Boundary Conditions

For the experimental setup described above and in Falanga et. al.¹ the tunnel run times were sufficiently long for the model temperatures to equilibrate and thus adiabatic wall boundary conditions are appropriate. However it is not clear that these conditions are appropriate for the full scale launch vehicle during the ascent phase of the launch. The free stream conditions change rapidly and it is not certain that adiabatic wall conditions are correct for a numerical simulation of a flight scenario. To determine the sensitivity of the PIFS to different types of boundary conditions computations were made to compare the effect of isothermal hot/cold wall to adiabatic wall boundary conditions. For the cold wall, the freestream test section

temperature was used as the surface temperature. For the hot wall, the tunnel stagnation temperature was used as the surface temperature. In the following sections, unless otherwise stated, adiabatic walls were simulated for the cases shown.

V. Results

V.A. Laminar Results

Simulated results were quantified by calculating X_s , θ_s , and δ_j . A comparison of separation distance from the nose and the angle of the boundary layer separation with the Langley tunnel data can be found in Fig. 5 with the corresponding data in Tables 3 and 4, respectively. The boundary layer separated at some point ahead of the flare-cylinder junction for all pressure ratios. This is in qualitative agreement with wind tunnel data. The streamline plots used to calculate X_s for the start of the separated region can be found in Fig. 7. The plots used for the shock extrapolation technique to determine X_s are shown in Figs. 8 (a) through 13 (a). The shock extrapolation technique consistently predicts a larger separated region as can be seen in Figs. 5 (a) and 6 for the laminar and fully turbulent flow predictions, respectively. The separation distance asymptotically approaches the cone-cylinder junction as the exit pressure ratio is increased. The laminar results appear to be separating more aggressively than indicated by the experimental data. The fully turbulent flow predictions indicate that turbulence completely suppresses the formation of a PIFS region and the SST model suppresses any kind of flow separation. This indicates that the flow is mostly laminar. The turbulent and transition results are discussed more completely in the next sections.

The initial inclination angle of the laminar flow jet is plotted as a function of $\frac{P_j}{P_\infty}$ in Fig. 14 with the data given in Table 5. Estimates of the initial inclination angle were generated using the results of Figs. 15 and 16. The magnitude of the density gradients $\sqrt{(\delta\rho/\delta x)^2 + (\delta\rho/\delta y)^2 + (\delta\rho/\delta z)^2}$ is very definitive in showing the plume flow features as shown in Fig. 16. To match the plume boundaries with the features shown in these figures, the experimental and computed Schlieren images of Figs. 8 through 13 were used. The experimental Schlieren images are with the knife edge placed horizontally. The CFD density gradients are in the vertical direction, i.e., $\delta\rho/\delta z$. The computed results show large difference between the initial inclination angle determined by the streamlines as opposed to those determined by the vertical density gradients.

In general the CFD results predict the general trend of the separation distance moving upstream as the nozzle exit pressure is increased. The trend of increasing separation angle with increased nozzle exit pressure ratio is also in agreement with the wind tunnel data. However, the detailed trend of the experimental separated region growth and initial plume inclination are not matched well by the laminar CFD predictions. The laminar flow assumption of the experimental report may not be correct, and will be discussed next.

V.B. Turbulent Results

Plots of the separation distance using both the shock extrapolation technique and the skin friction method can be found in Fig. 6. Five different combinations of the correction terms for the SST model are plotted. Condition 1 represents the case with only the compressibility correction, 2 only the curvature correction, 3 only the temperature correction, 4 is with all three corrections, and 5 is the basic SST model with all correction terms turned off. No dramatic differences are seen between the various correction terms. While the laminar results seem to over predict the extent of plume-induced flow separation, the fully turbulent results suppress the effect of the plume completely. That is, the separation point remains fixed for all exit pressure ratios. A large discrepancy also exists between the prediction of the separation point by the two turbulence models.

The SA model predicts the flow separation caused by the flare which acts to produce a larger separation region than found for the SST model. The SST model suppresses the effect of both the plume and the flare. Boundary layer profiles for the laminar and turbulent cases can be found in Fig. 17.

V.C. Transitional Flow Results

Plots of separation distance for the four transition locations can be found below in Fig. 18. As the trip location is moved further aft, the resulting solution approaches the laminar results. When the SA model is used for these cases, a trip location between stations two and three best represents the experimental results. For the SST model (with no correction terms), the best agreement lies when the trip location is

placed between locations one and two. These locations correspond to the region aft of the flare but before the midpoint on the nozzle, and the region between the midpoint of the flare before the end of the flare, respectively.

V.D. Effect of Isothermal Walls

A plot depicting the effect of changing the wall boundary condition from adiabatic to a hot wall isothermal and cold wall isothermal can be found in Fig. 19. The stagnation temperature in the wind tunnel was used for the hot wall isothermal while the test section static temperature was used for the cold wall isothermal case. The trip location was chosen to be station 3 as before with the SA model. This particular station was chosen arbitrarily. Again, the separation point was calculated using the shock extrapolation method mentioned earlier. From Fig. 19, the hot wall isothermal case is highly plume induced behaving in much the same way as the laminar results. The cold plume acts to suppress the effect of the plume completely and to a smaller extent suppress some of the separation from the flare (as can be seen at the lower exit pressure ratios).

Fig. 20 shows a comparison of the boundary layer profiles for the adiabatic, cold and hot wall isothermal cases at four different exit pressure ratios all taken at the midpoint of the cylinder. The results are in line with boundary layer theory in that the hot wall solution displays a thicker boundary layer and thinner profile (compared to the adiabatic wall temperature) which is more vulnerable to flow separation, while the cold wall boundary layer is thinner and has a fatter profile which is more resistant to flow separation.

VI. Conclusion

In general, for the laminar cases it was found that the large underexpanded plume produced from the nozzle moved the separation point further upstream when the nozzle exit pressure ratio was increased. The fully laminar results predict a large amount of plume induced flow separation than was found in the wind tunnel experiment. For the fully turbulent cases, the separation point remained fixed for all exit pressure ratios indicating no effect of the plume for these cases. The SA model predicted separation due to the flare. A laminar-turbulent transitional boundary layer seemed to produce the best agreement with the wind tunnel experiment. In particular, when the trip point was placed near the end of the flare, the best agreement was realized.

The hot wall isothermal case produced highly plume-induced flow while the cold wall isothermal case suppressed the plume effect. In addition, the measured point of separation on the body was dependent upon the method used. The shock extrapolation method consistently predicted a larger separated region than the skin friction method. In general, it was found that plume-induced flow separation is highly sensitive to wall boundary conditions, turbulence model, and exit pressure ratio. Thus, in general, for laminar flows the CFD code OVERFLOW closely predicts the extent of flow separation triggered by a plume.

Acknowledgments

Special thanks to Jeff Onufer, William Chan, and Henry Lee for all of their time and help on this project.

References

- ¹Falanga, Ralph A.; *Exploratory Tests of the Effects of Jet Plumes on the Flow Over Cone-Cylinder-Flare Bodies*, NASA TN D-1000, Langley Research Center, Hampton, VA, 23681, 1962.
- ²Boggess, Jr., Andrew L.; *An Investigation of the Unsteady Flow Associated with Plume Induced Flow Separation*, BER Report No. 149-02., Langley Research Center, Hampton, VA, 23681, 1972.
- ³Bender, Robert, and Canabal, Francisco; *CLV-5 Plume Induced Flow Separation (PIFS)*, Unpublished Presentation, Marshall Space Flight Center, Huntsville, AL, xxxxx, 2006.
- ⁴Gusman, M., Housman, J., and Kiris, C.; *Best Practices for CFD Simulations of Launch Vehicle Ascent with Plumes - OVERFLOW Perspective*, 49th AIAA Aerospace Sciences Meeting, Orlando, FL, January 2011. (submitted for publication).
- ⁵Deere, Karen, Elmiligui, Alaa, and Abdol-Hamid, K.S.; *USM3D Simulations of Saturn V Plume Induced Flow Separation*, 49th AIAA Aerospace Sciences Meeting, Orlando, FL, January 2011. (submitted for publication).
- ⁶P. G. Buning, D. C. Jespersen, T. H. Pulliam, G. H. Klopfer, W. M. Chan, J. P. Slotnick, S. E. Krist, and K. J. Renze; *OVERFLOW Users Manual*, NASA Unpublished Report, 2005.
- ⁷NASA's *Exploration System Architecture Study*, NASA-TM-2005-214062, November 2005.

⁸Chan, William.; *The OVERGRID Interface for Computational Simulations on Overset Grids*, AIAA Paper 2002-3188, 32nd AIAA Fluid Dynamics Conference and Exhibit, St. Louis, MO, June 2002.

⁹Chan, W. M., Gomez, R. J., Rogers, S. E., Buning, P. G. *Best Practices in Overset Grid Generation*, AIAA Paper 2002-3191, June 2002.

¹⁰Jackson, Charlie M. Jr., Corlett, William A., and Monta, William J.; *Description and Calibration of the Langley Unitary Plan Wind Tunnel*, NASA LaRC TP-1905, Hampton, VA, 23681, 1981

Table 1. Free-stream flow conditions.

| M_∞ | $T_\infty(^{\circ}R)$ | γ_∞ | $P_\infty(\text{psi})$ | $\rho_\infty(\frac{\text{lbm}}{\text{ft}^3})$ | $Re_{l,\infty}$ |
|------------|-----------------------|-----------------|------------------------|---|-----------------|
| 4.65 | 114.5 | 1.4 | 0.2 | 0.000465 | 407,610 |

Table 2. Mesh dimensions.

| Zone | J_{max} | K_{max} | L_{max} | Total |
|---------------|-----------|-----------|-----------|-----------|
| Near Body | 983 | 301 | 3 | 887,649 |
| Nozzle | 267 | 135 | 3 | 108,135 |
| Nozzle Collar | 231 | 83 | 3 | 57,519 |
| Plume | 296 | 505 | 3 | 448,440 |
| Outer Box | 1,429 | 333 | 3 | 1,427,571 |

Table 3. Separation distance from nose of model (inches). Laminar flow with adiabatic wall boundary conditions.

| P_j/P_∞ | $X_s(\text{Streamlines})$ | $X_s(\text{ShockExtrapolation})$ | $X_s(\text{Experiment})$ |
|----------------|---------------------------|----------------------------------|--------------------------|
| 0 | 3.43 | 2.97 | N/A |
| 13 | 3.40 | 2.98 | 3.0±0.05 |
| 36 | 2.52 | 2.25 | 3.01±0.05 |
| 73 | 2.41 | 2.15 | 2.85 ±0.05 |
| 127 | 2.33 | 2.08 | 2.25±0.05 |
| 168 | 2.32 | 2.07 | N/A |

Table 4. Separation angle (degrees). Laminar flow with wall adiabatic boundary conditions.

| P_j/P_∞ | $\theta_s(\text{CFD})$ | $\theta_s(\text{Experiment})$ |
|----------------|------------------------|-------------------------------|
| 13 | 4.99 | 4.0±0.25 |
| 36 | 7.61 | 5.0±0.25 |
| 73 | 7.83 | 4.5±0.25 |
| 127 | 8.34 | 8.5±0.25 |
| 168 | 8.56 | 9.0±0.25 |

Table 5. Initial plume inclination angle δ_j (degrees). Laminar flow with adiabatic boundary conditions.

| P_j/P_∞ | CFD(streamlines) | CFD(density gradient) | Experiment |
|----------------|------------------|-----------------------|------------|
| 13 | 57.01 | 40 | 34±5 |
| 36 | 61.72 | 49 | 46±5 |
| 73 | 73.59 | 65 | 59±5 |
| 127 | 82.53 | 68 | 66±5 |
| 168 | 82.13 | 67 | 68±5 |

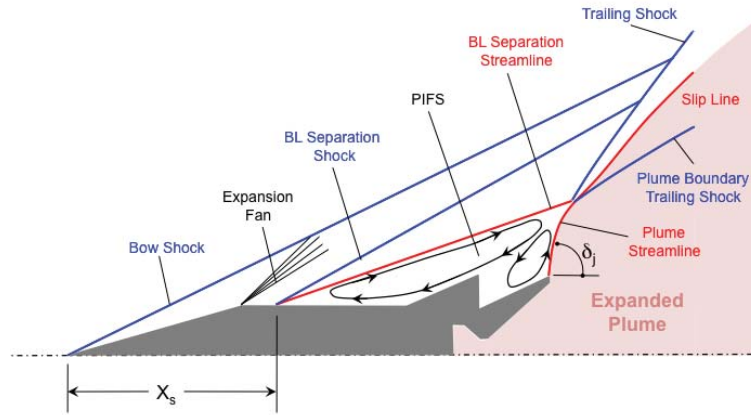


Figure 1. Plume Induced Flow Separation (PIFS).

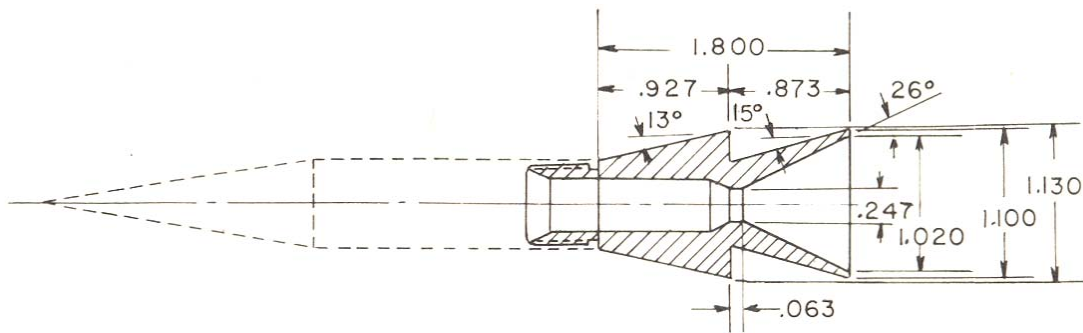


Figure 2. Schematic of configuration $\frac{l}{d}=8.28$ $M_j=4.53$ $l=5.823$ in.

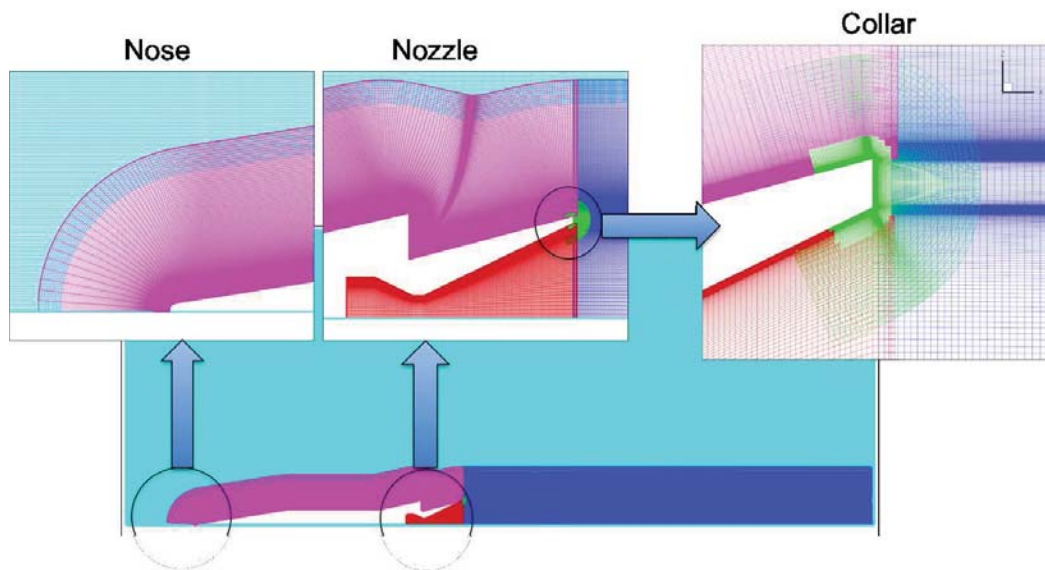


Figure 3. Overset mesh, 5 zones, 2.9 million grid points.

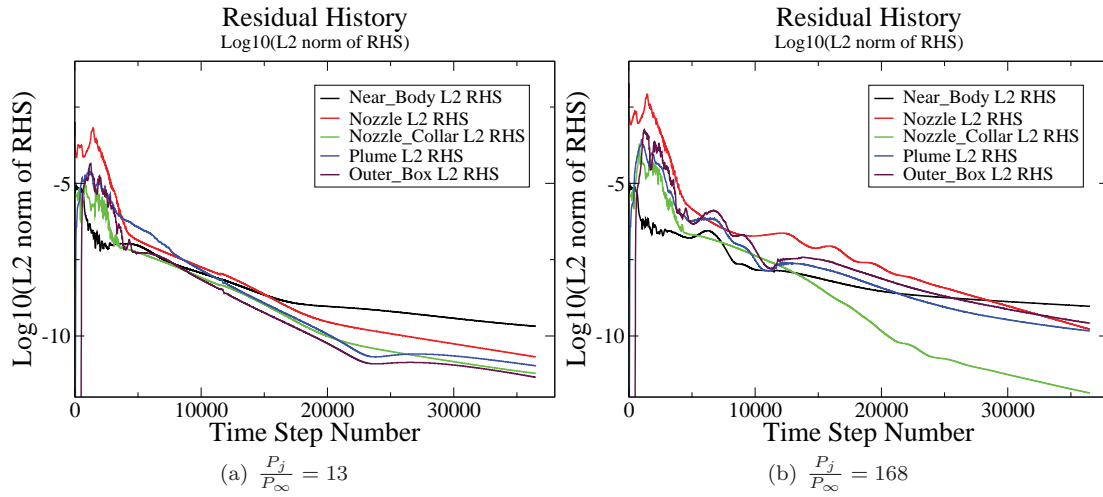


Figure 4. Residual history for laminar cases.

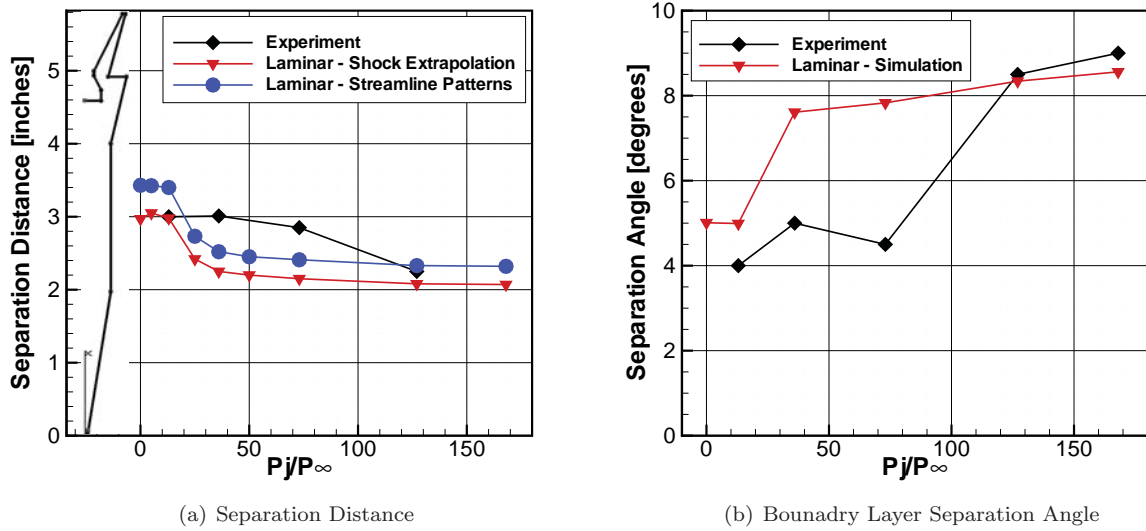
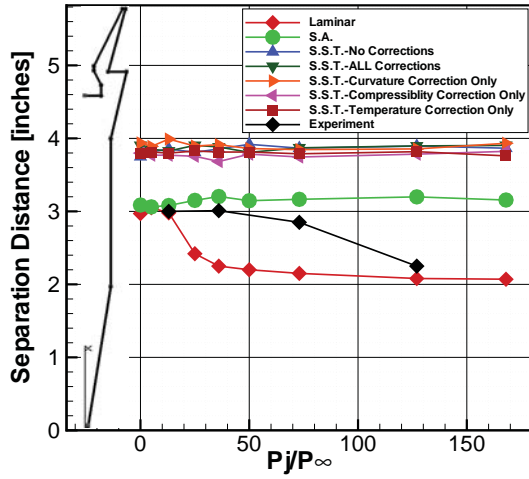
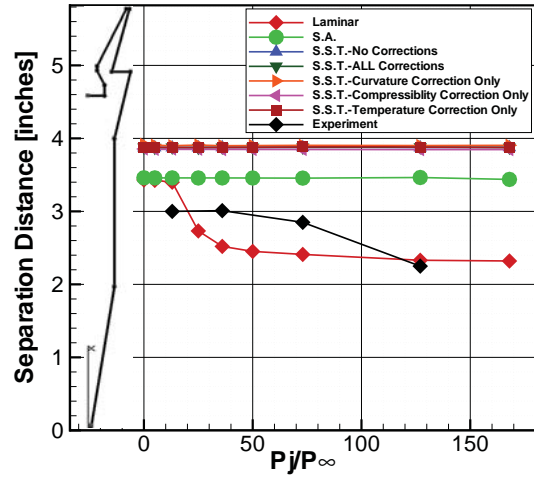


Figure 5. Separation parameters: laminar flow simulations vs experiment.

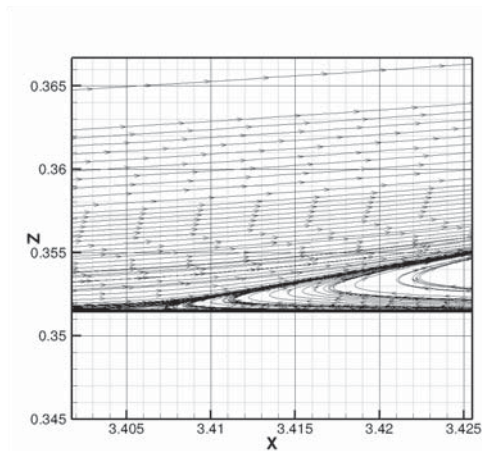


(a) Shock Extrapolation Method

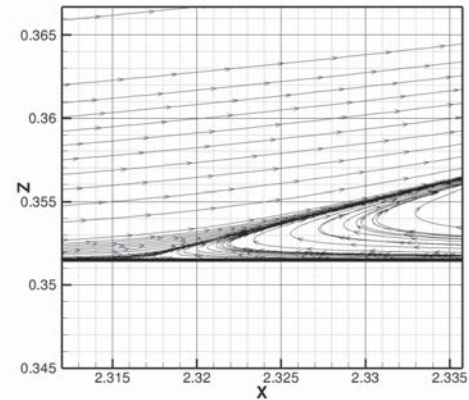


(b) Skin Friction Method

Figure 6. Two different methods of measuring the separation distance: laminar/turbulent simulations vs experiment.

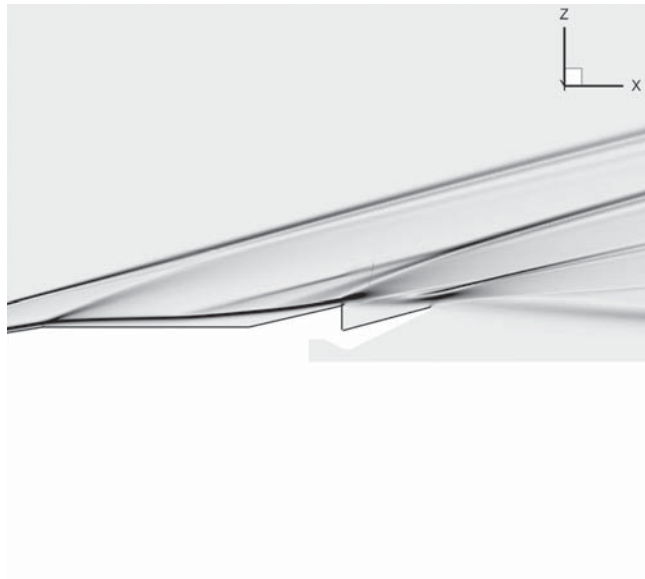


(a) $\frac{P_j}{P_\infty} = 13$

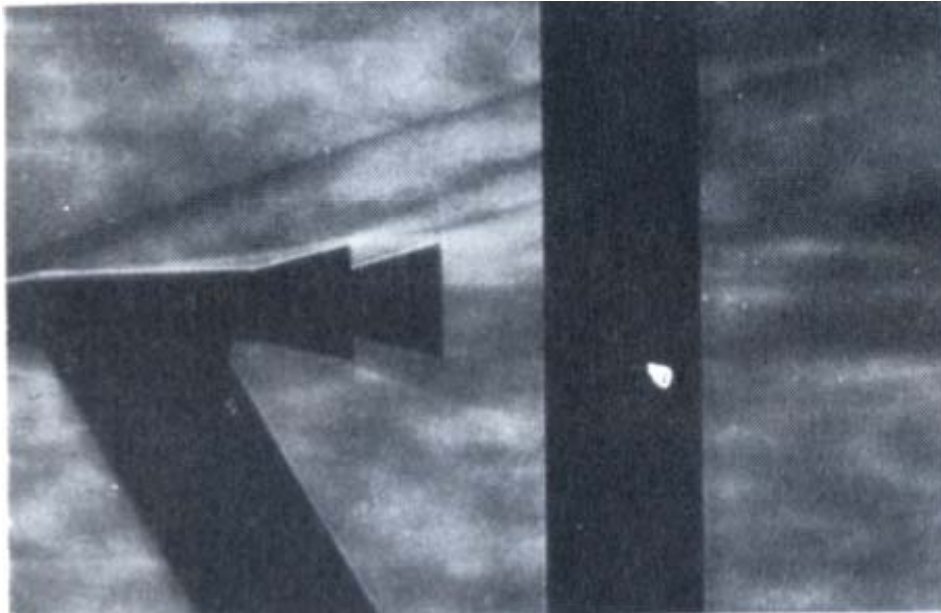


(b) $\frac{P_j}{P_\infty} = 168$

Figure 7. Streamlines in separation region for laminar flow with adiabatic boundary conditions.

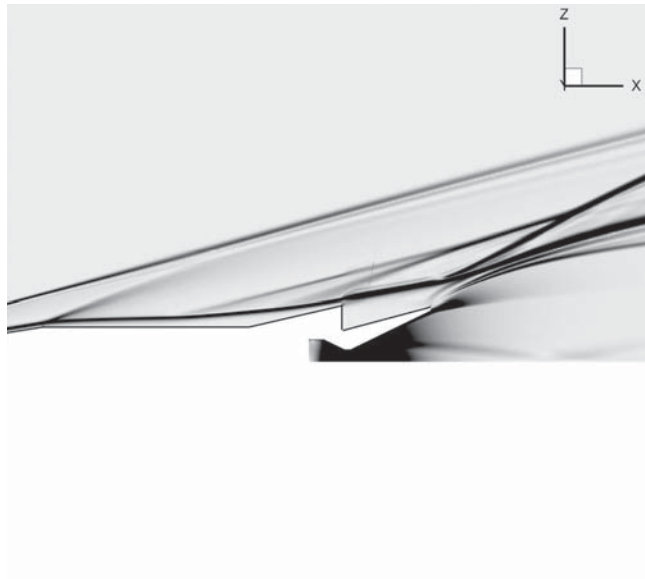


(a) CFD

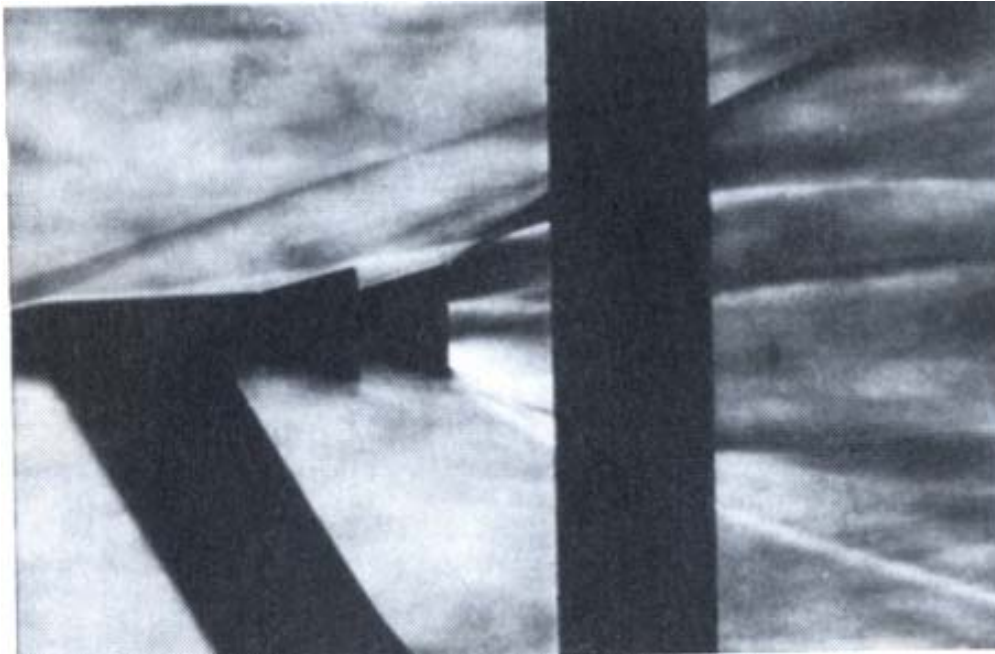


(b) Experiment

Figure 8. Comparison of CFD density gradient view with the experimental Schlieren image for the jet off case. Laminar flow with adiabatic boundary conditions.

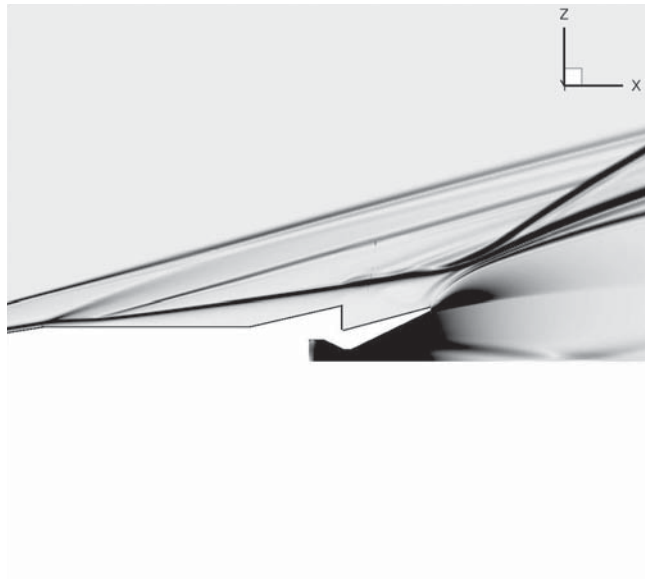


(a) CFD

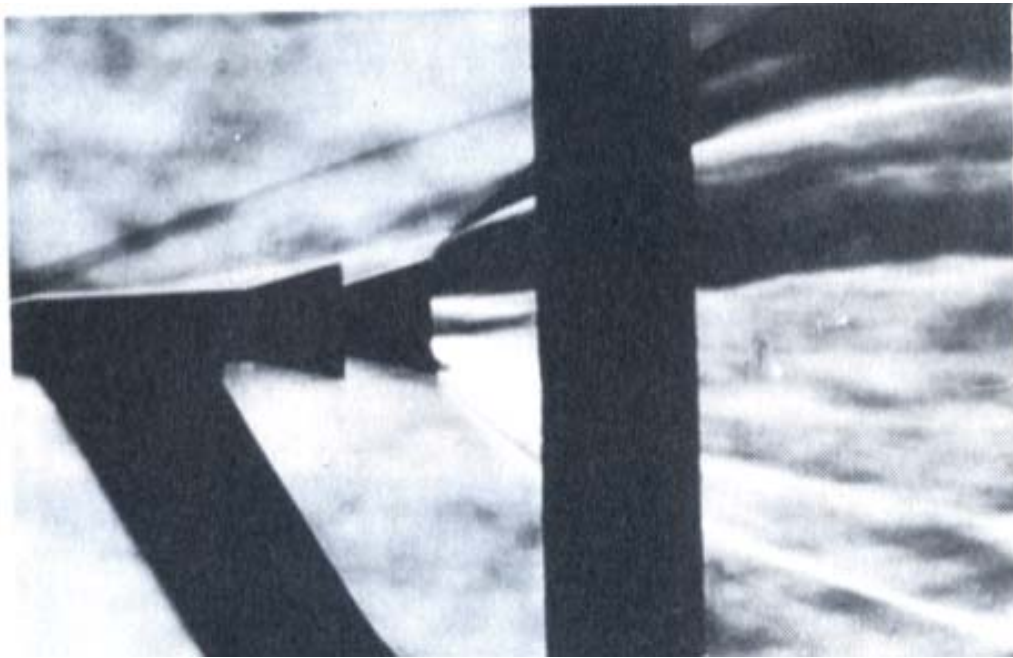


(b) Experiment

Figure 9. Comparison of CFD density gradient view with the experimental Schlieren image for the nozzle pressure ratio, $\frac{P_j}{P_\infty} = 13$. Laminar flow with adiabatic boundary conditions.

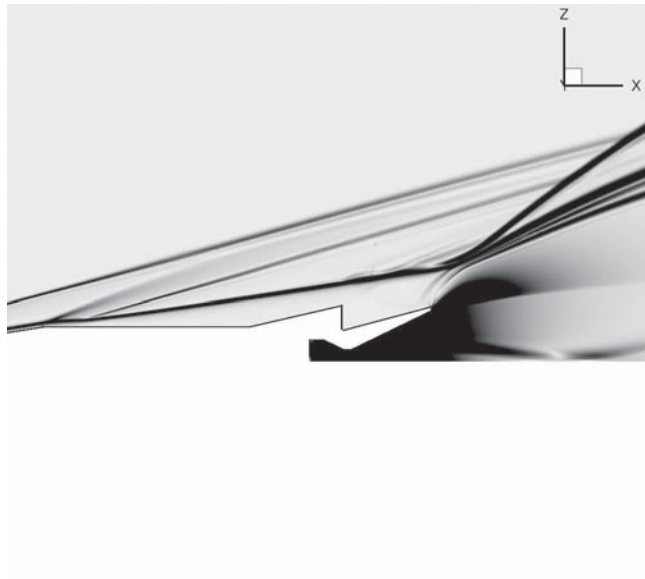


(a) CFD

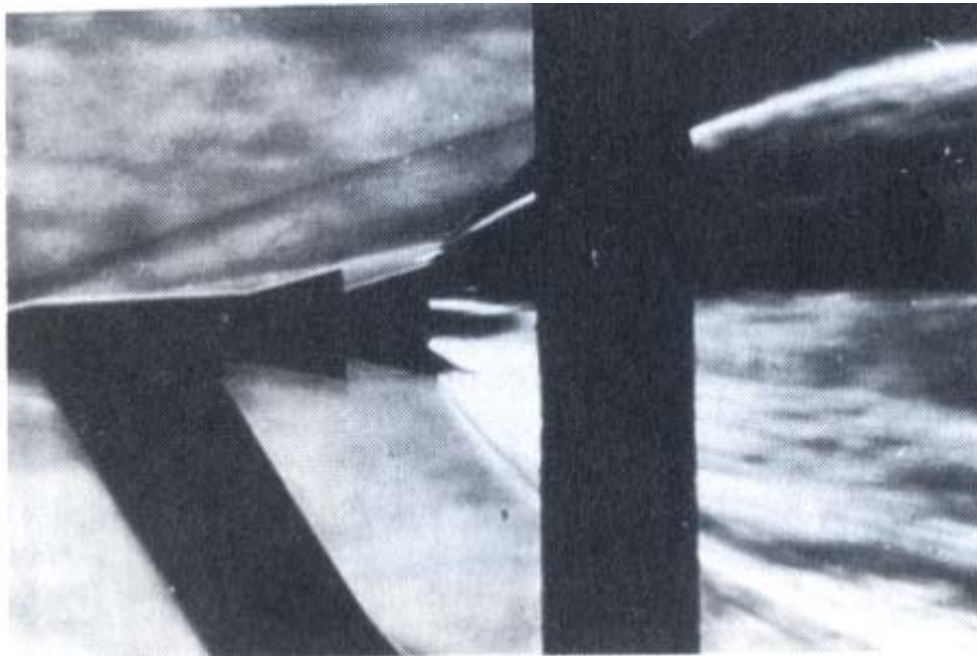


(b) Experiment

Figure 10. Comparison of CFD density gradient view with the experimental Schlieren image for the nozzle pressure ratio, $\frac{P_j}{P_\infty} = 36$. Laminar flow with adiabatic boundary conditions.

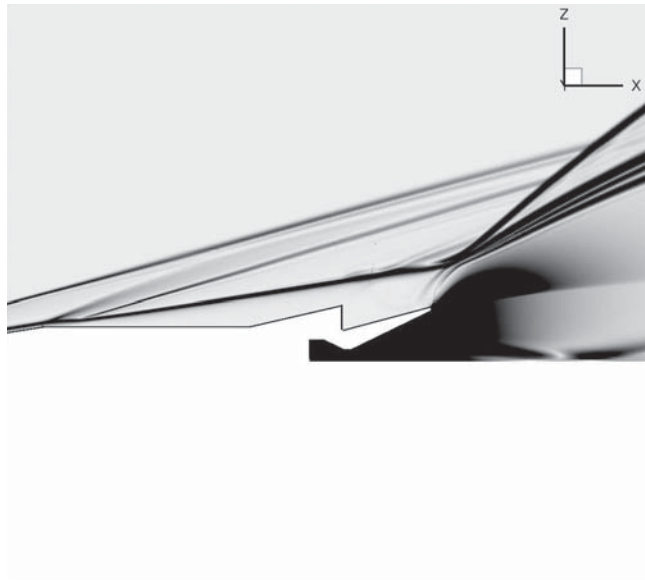


(a) CFD

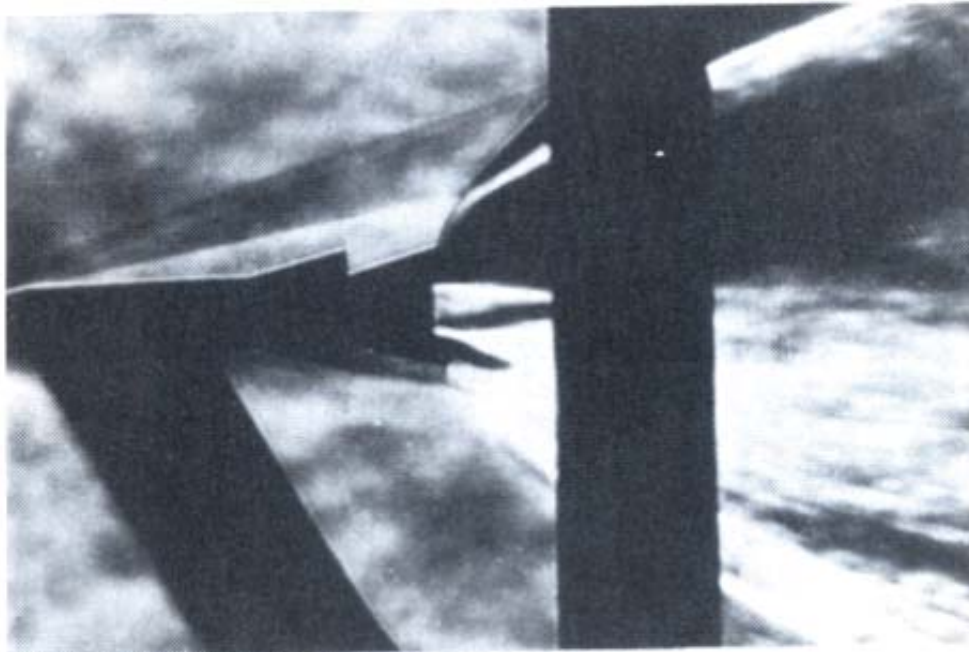


(b) Experiment

Figure 11. Comparison of CFD density gradient view with the experimental Schlieren image for the nozzle pressure ratio, $\frac{P_j}{P_\infty} = 73$. Laminar flow with adiabatic boundary conditions.

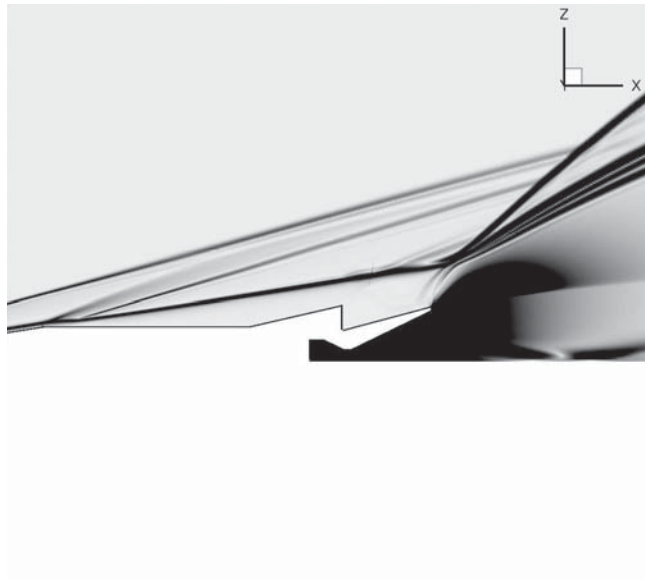


(a) CFD

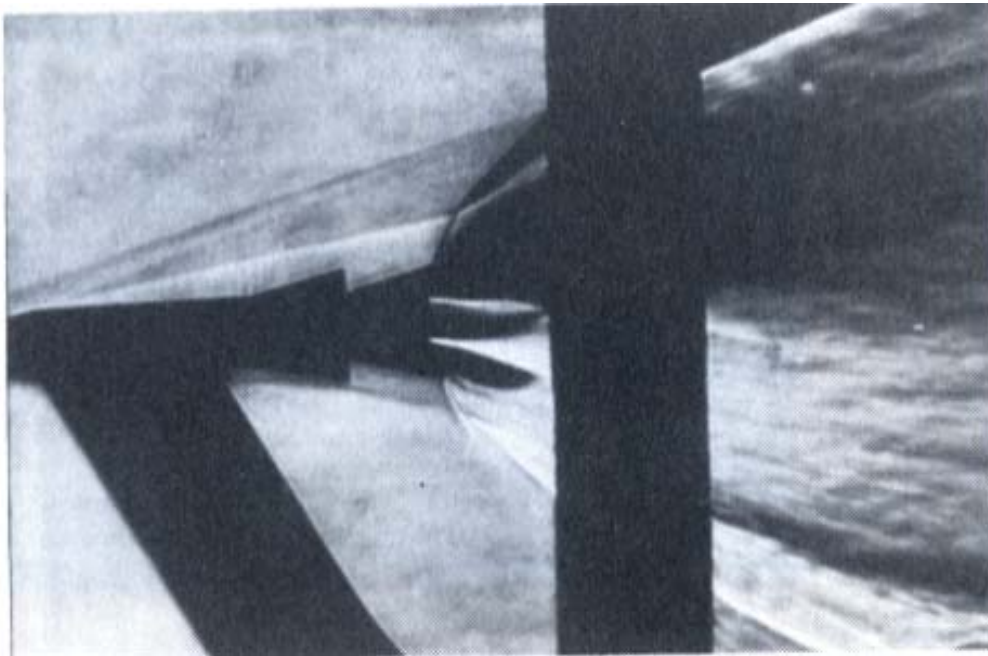


(b) Experiment

Figure 12. Comparison of CFD density gradient view with the experimental Schlieren image for the nozzle pressure ratio, $\frac{P_j}{P_\infty} = 127$. Laminar flow with adiabatic boundary conditions.



(a) CFD



(b) Experiment

Figure 13. Comparison of CFD density gradient view with the experimental Schlieren image for the nozzle pressure ratio, $\frac{P_j}{P_\infty} = 168$. Laminar flow with adiabatic boundary conditions.

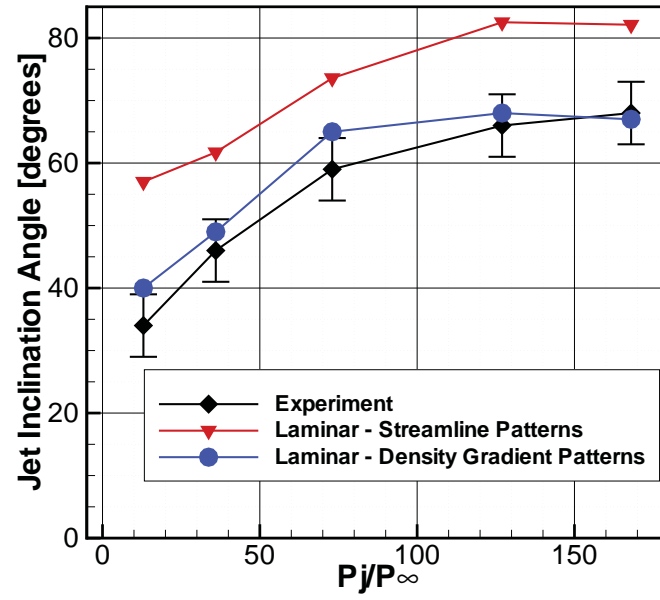


Figure 14. Initial plume inclination angle (degrees) for laminar flow with adiabatic boundary conditions.

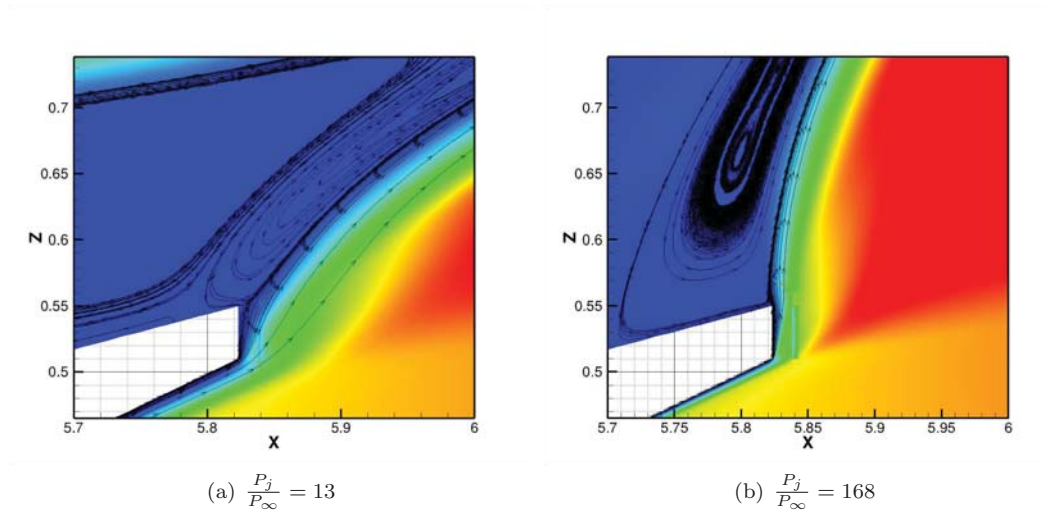


Figure 15. Streamlines in plume region for laminar flow with adiabatic boundary conditions.

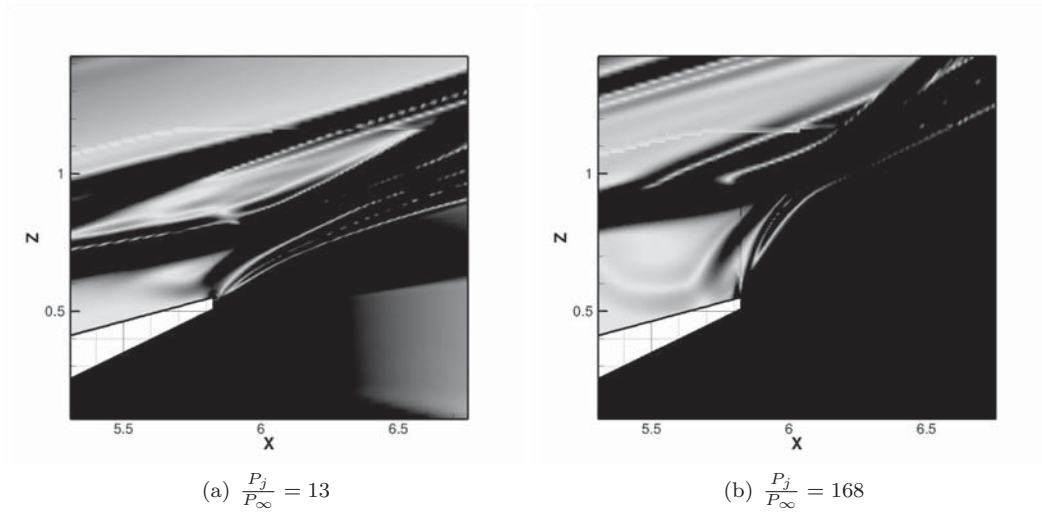


Figure 16. Density gradient magnitude in plume region for laminar flow with adiabatic boundary conditions.

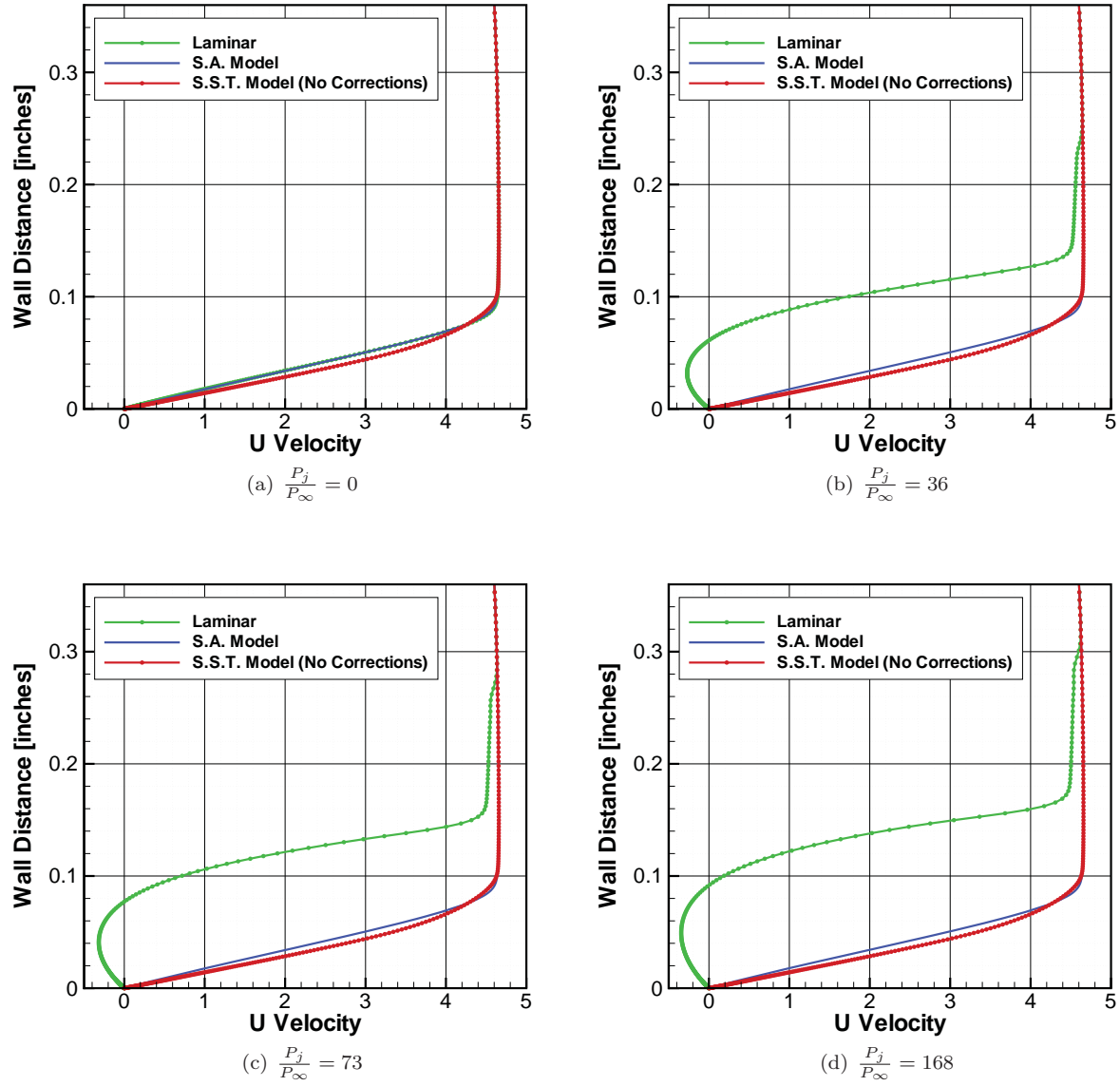
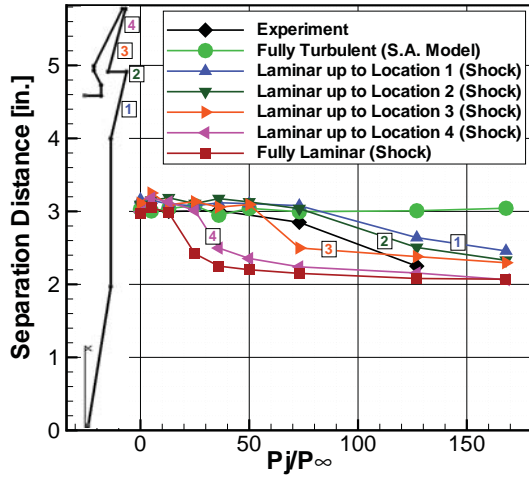
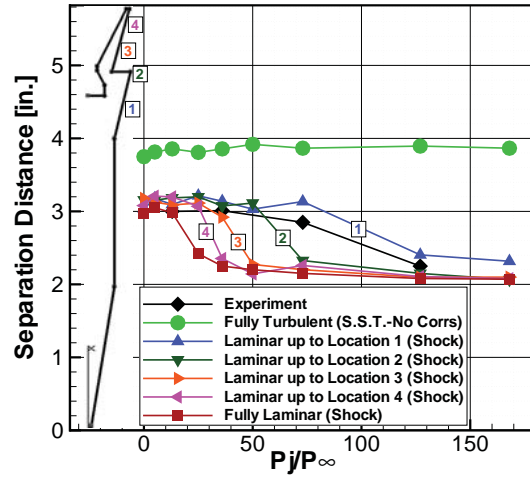


Figure 17. Effect of different turbulence models on boundary layer profiles at the midpoint of cylinder for selected nozzle pressure ratios.



(a) SA for turbulent regions



(b) SST for turbulent regions

Figure 18. Separation distance comparisons of experiment vs laminar/turbulent flow simulations with 4 transition locations. Separation distance measured by shock extrapolation only.

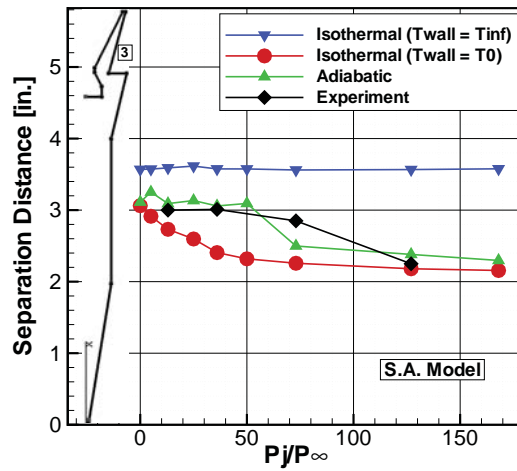


Figure 19. Adiabatic/isothermal wall boundary condition comparisons with experiment.

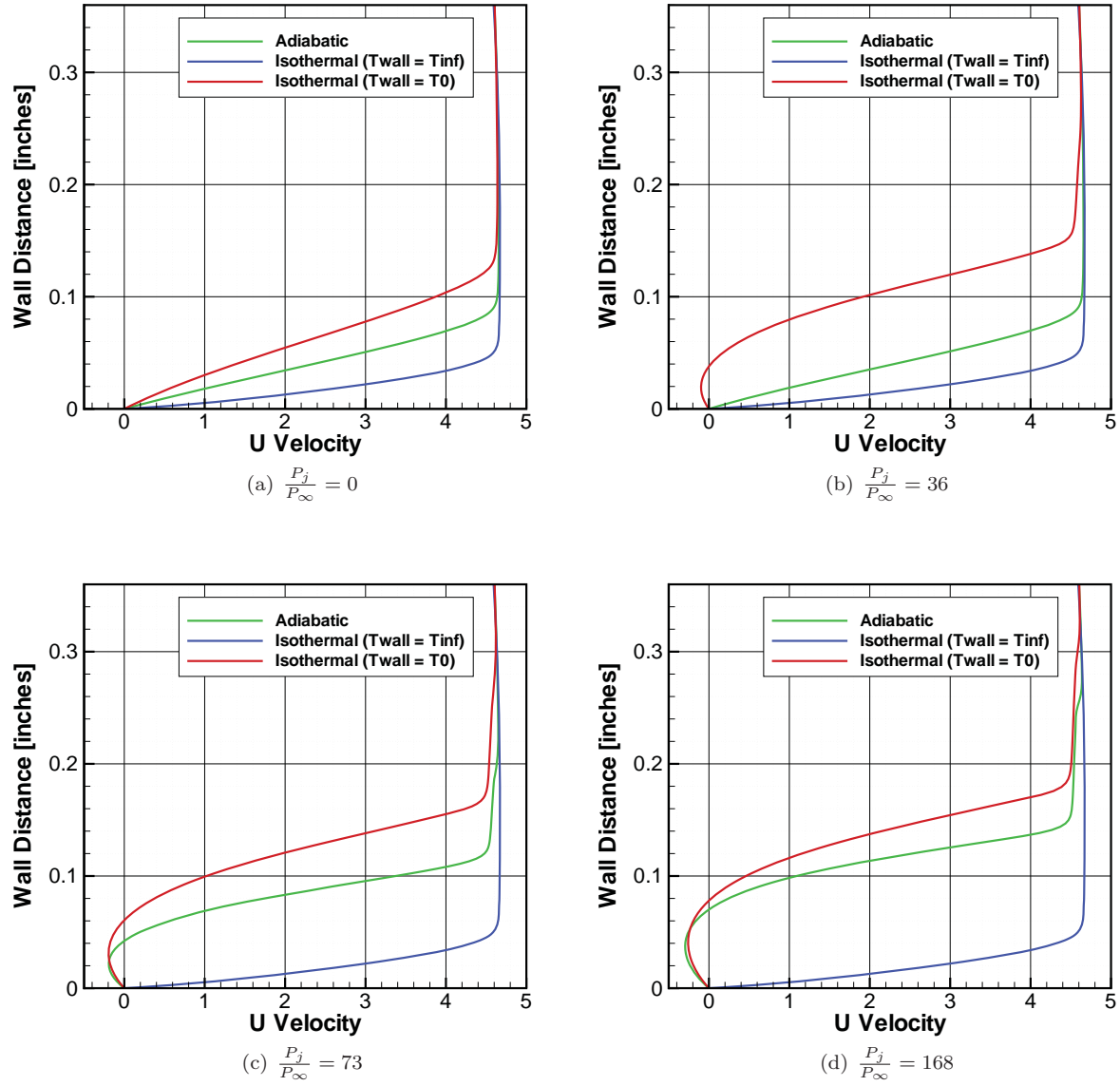


Figure 20. Effect of different wall boundary conditions on boundary layer profiles at the midpoint of cylinder for selected nozzle pressure ratios.